



RESEARCH ARTICLE

10.1002/2016JC012541

On the effect of topography and wind on warm water inflow—An idealized study of the southern Weddell Sea continental shelf system

Key Points:

- PV constraints impede warm inflow to a coastal deep trough
- Warm inflow along the trough decreases with stronger wind
- Dense water formation increases on-shelf transport of WDW

Supporting Information:

- Supporting Information S1
- Movie S1
- Movie S2
- Movie S3

Correspondence to:

K. Daae,
kjersti.daae@uib.no

Citation:

Daae, K., T. Hattermann, E. Darelius, and I. Fer (2017), On the effect of topography and wind on warm water inflow—An idealized study of the southern Weddell Sea continental shelf system, *J. Geophys. Res. Oceans*, 122, 2622–2641, doi:10.1002/2016JC012541.

Received 8 NOV 2016

Accepted 28 FEB 2017

Accepted article online 2 MAR 2017

Published online 31 MAR 2017

© 2017. The Authors.

This is an open access article under the terms of the Creative Commons Attribution-NonCommercial-NoDerivs License, which permits use and distribution in any medium, provided the original work is properly cited, the use is non-commercial and no modifications or adaptations are made.

K. Daae¹ , T. Hattermann^{2,3} , E. Darelius¹ , and I. Fer¹

¹Geophysical Institute, University of Bergen and Bjerknes Centre for Climate Research, Bergen, Norway, ²Akvaplan-niva AS, High North Research Centre, Tromsø, Norway, ³Helmholtz Centre for Polar and Marine Research, Alfred Wegener Institute, Bremerhaven, Germany

Abstract An idealized eddy-resolving numerical model, with topographic features common to the southern Weddell Sea, is constructed to study mechanisms through which warm deep water enters a wide continental shelf with a trough. The open ocean, represented by a 1700 m deep channel, is connected to a 400 m deep shelf with a continental slope. The shelf is narrow (50 km) in the east but widens to 300 km at the center of the model domain. Over the narrow shelf, the slope front is balanced by wind-driven Ekman downwelling and counteracting eddy overturning, favoring on-shelf transport of warm water in summer scenarios when fresher surface water is present. Over the wide shelf, the Ekman downwelling ceases, and the mesoscale eddies relax the front. Inflow of warm water is sensitive to along-shelf salinity gradients and is most efficient when denser water over the wide shelf favors up-slope eddy transport along isopycnals of the V-shaped slope front. Inflow along the eastern side of the trough cannot penetrate the sill region due to potential vorticity constraints, while along the western trough flank, eddy-induced inflow crosses the sill and reaches the ice front. The warm inflow into the trough is sensitive to the density of the outflowing dense shelf water. For weaker winds, absence of the dense water outflow leads to a reversal of the trough circulation and a strong inflow of warm water, while for stronger winds, baroclinic effects become less important and the inflow is similar to experiments including dense water outflow.

1. Introduction

The observed thinning of the floating ice shelves in West Antarctica has been attributed to increased basal melt caused by increased flow of warm ($> -1.9^{\circ}\text{C}$) Circumpolar Deep Water (CDW) into the ice shelf cavities [Pritchard *et al.*, 2012]. Ice shelf thinning reduces buttressing of the ice sheet upstream, resulting in accelerated ice flow and ice sheet mass loss [Dupont and Alley, 2005]. The ice shelf thinning is strongest in the Bellingshausen and Amundsen Sea [Pritchard *et al.*, 2012; Paolo *et al.*, 2015], where CDW has direct access to the ice shelf cavities [Jacobs *et al.*, 2011].

In other regions, such as the Ross Sea and the Weddell Sea, water temperatures on the continental shelf and inside the ice shelf cavities are close to the surface freezing point (-1.9°C) [Nicholls *et al.*, 2009; Orsi and Wiederwohl, 2009], and the basal melt rates are low ($\sim 0.13 \text{ m yr}^{-1}$) [Rignot *et al.*, 2013]. The warm CDW ($> 1.25^{\circ}\text{C}$) is decoupled from the shelf circulation by a front system over the continental slope, often referred to as the Antarctic Slope Front (ASF), and characterized by a southward depression of the isopycnals toward the continental slope [Gill, 1973; Jacobs, 1991]. Dense water formation over the continental shelf in the southern Weddell Sea [Nicholls *et al.*, 2009; Foster and Carmack, 1976], where the large Filchner-Ronne Ice Shelf (FRIS) resides (Figure 1), furthermore leads to a second, on-shore front separating the lighter water in the north from the dense shelf water. The isopycnals over the shelf break and the continental slope thus exhibit a V-shape [Jacobs, 1991; Gill, 1973].

In the Weddell Sea, the ASF impedes on-shore transport of warm deep water (WDW), a slightly cooler and fresher derivative of CDW [Heywood *et al.*, 1998]. However, future climate model simulations [Hellmer *et al.*, 2012; Timmermann and Hellmer, 2013] suggest circulation changes in which WDW will access the FRIS cavity and increase melting from 0.2 to almost 4 m/yr within this century. The predicted increase in the flow of WDW toward the FRIS is linked to the Filchner Depression (FD) and changes in the momentum transfer from the atmosphere to the ocean, which causes a redirection of the slope current.

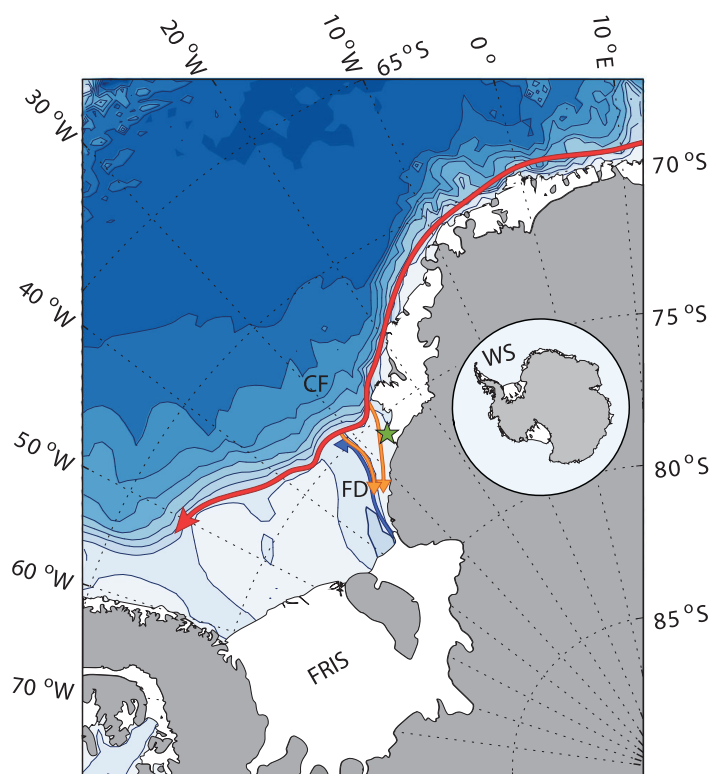


Figure 1. Map of the southern Weddell Sea. Bathymetric contours are drawn every 500 m. The Cray Fan (CF), Filchner-Ronne Ice Shelf (FRIS), and Filchner Depression (FD) are indicated by bold letters, and Halley Research Station is marked by a green star. The red arrow shows the slope current, the orange arrows show the coastal current and the inflow through the depression, while the blue arrow shows the overflow. An inset shows the Antarctic continent, with the Weddell Sea (WS) in the top left sector.

The slope current is associated with the offshore part of the ASF [Gill, 1973] and flows westward along the continental slope. In the eastern Weddell Sea, where the continental shelf is a few kilometers wide, the slope current coincides with the Antarctic Coastal Current (red arrow in Figure 1), but as the continental shelf widens at 27°W and the coast separates from the continental slope, the current bifurcates into a coastal current (orange arrow in Figure 1) and the slope current [Whitworth *et al.*, 1985; Heywood *et al.*, 1998]. Downstream of the bifurcation, the Filchner Depression, a 100 km wide and 1000 m deep coastal trough with a sill depth of about 600 m, crosscuts the wide continental shelf. The FD is filled with dense Ice Shelf Water (ISW) that emerges from the FRIS cavity and spills over the FD sill at a rate of 1.6 Sv (blue arrow in Figure 1) [Foldvik *et al.*, 2004].

Existing climate model simulations do not fully resolve the relevant dynamics nor provide clear

answers on the processes being responsible for the predicted circulation changes. The on-shore heat transport across the ASF can potentially be controlled by several mechanisms. This includes flow instability of the slope current [Klinck and Dinniman, 2010], thermocline response to surface wind stress and near-surface hydrographic conditions [Hattermann *et al.*, 2014], mesoscale eddies [Nøst *et al.*, 2011; Stewart and Thompson, 2015], and flow interaction with bottom corrugations and troughs crosscutting the shelf break [Klinck and Dinniman, 2010; St. Laurent *et al.*, 2013]. A better understanding of these mechanisms and the interplay between them is needed in order to improve future predictions of ice shelf-ocean interaction and ice sheet mass loss in a warming climate.

Model resolution is an important issue in studies of water exchange across the Antarctic continental slope, where the internal Rossby radius of deformation typically is less than 10 km. High resolution is required in order to properly resolve the steep topography and the water transport associated with mesoscale eddies [St. Laurent *et al.*, 2013; Stewart and Thompson, 2015], but are yet too computationally expensive to be applied over large areas and/or time scales. High-resolution idealized models, such as the one being used in this study, are therefore important tools to study mechanisms for on-shelf transport of warm water.

We investigate a shelf region similar to the southern Weddell Sea, using an eddy-resolving regional ocean model with idealized topography, hydrography, and forcing conditions. The geometry represents the essential features of the region; a steep continental slope ($\alpha=0.016$) connecting the deep ocean (1700 m) to a shallow (400 m) continental shelf, which is narrow in the east and opens up and widens toward the west. A deep coastal trough (sill depth 600 m), representing the FD (Figure 1), cuts across the wide shelf (Figure 2a). We study the slope front stability and the mechanisms which transport warm water on-shore over three bathymetric regions (narrow shelf, wide shelf, and trough opening).

It has been hypothesized that on-shelf transport of heat across the ASF, along the Weddell Sea continental slope, is controlled by a balance between the wind-driven Ekman overturning and a counteracting eddy

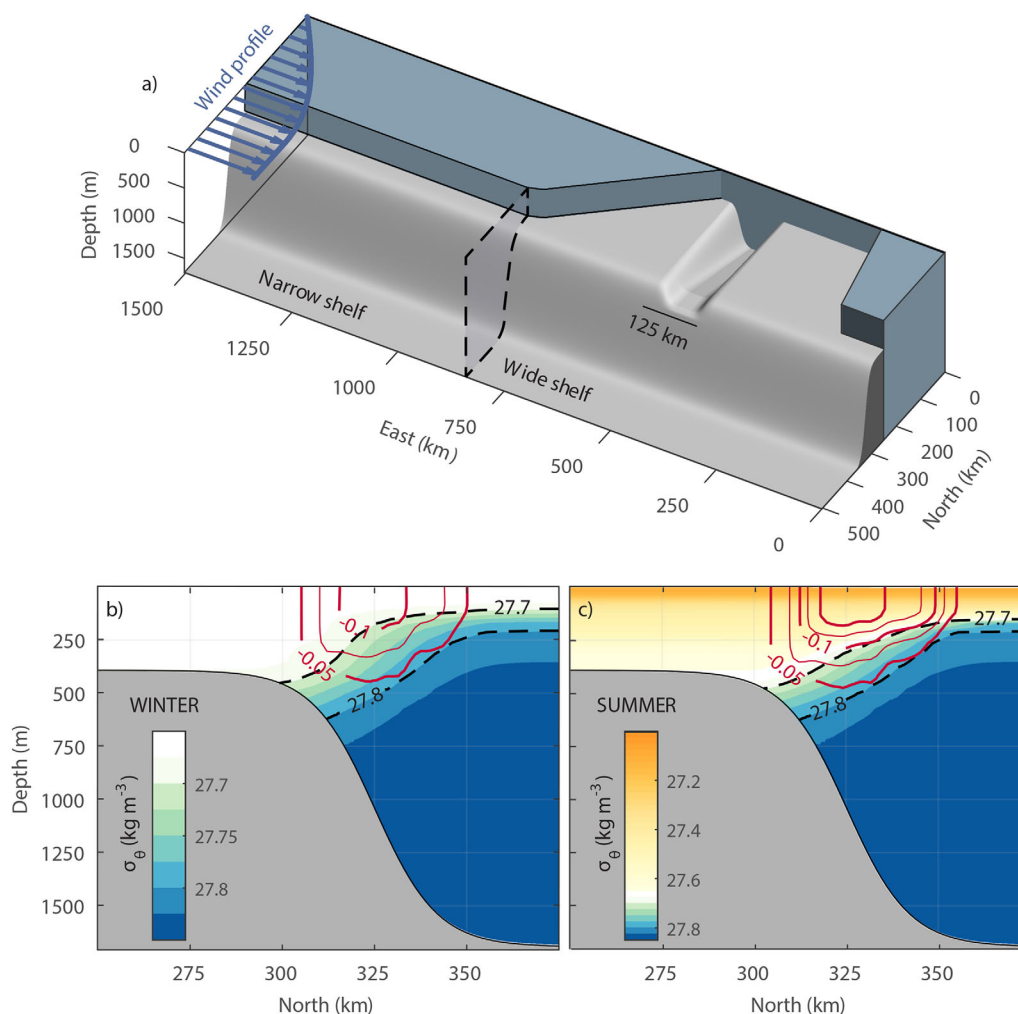


Figure 2. (a) Idealized model configuration. The shaded transect at 850 km East marks the transition from the narrow to the wide shelf. A 125 km wide trough cuts across the wide shelf region, with a sill depth of 600 m. The depth of the trough increases linearly to 900 m at the southern boundary. The zonal wind profile is shown with blue arrows. Potential density climatology for (b) winter and (c) summer, with geostrophic current velocity displayed as red contours. The winter climatology is also the same as the initial condition. $\sigma_\theta = 27.7$ and 27.8 isopycnals are shown with black dashed contours.

overturning [Nøst *et al.*, 2011]. However, previous modeling studies have mainly focused on zonally uniform, near equilibrium configurations [Stewart and Thompson, 2015]. We explore how this balance changes when the shelf widens. We perform a series of sensitivity tests to study the effect of (I) the magnitude of westward wind stress, (II) the shelf salinity, and (III) the surface hydrography.

Troughs across the continental shelf break offer pathways for shoreward transport of warm water. Observations from the FD show inflow of warm water with a core at 400 m depth along the eastern flank [Carmack and Foster, 1977; Foldvik *et al.*, 1985; Årthun *et al.*, 2012] during summer, which at least occasionally reaches as far south as the Filchner Ice Front and which appears to be wind driven [Darelius *et al.*, 2016]. Interactions between a shelf break jet and cross-shelf trough will depend on the trough geometry, stratification, and the strength and direction of the flow [Williams *et al.*, 2001; Klinck, 1996; Allen and Durrieu de Madron, 2009; Zhang *et al.*, 2011a].

We investigate how the southward transport of warm water in a trough, with characteristics similar to FD, responds to changes in forcing conditions I–III above. In addition, we explore (IV) how the presence of dense shelf water (DSW), a mixture of ISW and High Salinity Shelf Water, in the trough, and also the DSW density, affects the WDW inflow. Hellmer *et al.* [2017] suggested that the density of the ISW is an important regulator of the warm inflow. This work provides an assessment of the mechanisms they proposed.

The paper is organized as follows. Section 2 introduces relevant concepts of mesoscale eddy transports and potential vorticity constraints that are used to analyze the model results. The model results are presented in section 3, and a discussion of the model performance and limitations is given in section 4. Finally, a summary of the main findings is provided in section 5.

2. Methods

2.1. Model Setup

We conduct idealized numerical simulations using the Regional Ocean Modeling System (ROMS, version 3.6) [Shchepetkin and McWilliams, 2009]. The model domain is 1500 km \times 500 km, with a horizontal resolution of 1.5 km, which has previously been found to be sufficient to resolve cross-shelf transport by eddies [Hattermann *et al.*, 2014]. In the vertical, the model is discretized into 30 terrain-following layers with enhanced resolution near the surface and near the sea bed. The layer thickness varies from less than 3 m in the surface layer over the continental shelf up to 110 m in the deep ocean interior.

The idealized model geometry is shown in Figure 2a, resembling the prominent features of the southern Weddell Sea (Figure 1). The deep ocean is connected to a 400 m deep shelf with a continental slope, represented by a hyperbolic tangent function. The slope steepness ($\alpha = 0.016$) is similar to the Cray Fan region north of the FD (Figure 1). The maximum bottom depth in the open ocean is limited to 1700 m, which is assumed to cover the dynamically active part of the water column, while optimizing model performance, which is limited by the barotropic wave speed \sqrt{gH} . A 125 km wide trough, with geometry similar to FD, is crosscutting the continental shelf and the upper part of the continental slope. The trough deepens linearly from 600 m at the shelf break sill to 900 m at the southern boundary. The side walls are symmetric with steepness ($\alpha_{\text{trough}} = 0.0043\text{--}0.0109$ from the sill to the southern boundary) representative of the eastern flank of FD.

Horizontal advection of tracers and momentum are computed using a third-order upwind scheme with no explicit mixing being applied. The model is stepped forward in time with a split-explicit scheme, using a baroclinic time step of 3 min, and 25 barotropic substeps.

Initial and climatology hydrographic forcing (Figures 2b and 2c) are constructed from 26 conductivity-temperature-depth (CTD) profiles, taken across the eastern Weddell Sea continental shelf break at 17°W [Nøst and Lothe, 1997], and from more than 2000 CTD profiles from instrumented southern Elephant seals [Nøst *et al.*, 2011]. The dataset is described in Hattermann *et al.* [2014] and is adapted to the idealized setup, where we apply zonally homogeneous conditions. For our reference simulations, the trough is initially filled with DSW with temperature $\theta_{DSW} = -2^\circ\text{C}$ and salinity $S_{DSW} = 34.65$. These values fall within the range of observed DSW properties (Figure 3). At the southern boundary, we restore temperature and salinity to the initial values. We further impose a northward flux (~ 1 Sv), by restoring the velocity in the deep trough to $V_{\text{north}} = 0.025$ m s⁻¹ below 430 m, to ensure that the DSW properties do not drift over the 5 years we run the model. The restoring velocity is kept constant in all experiments, including those where DSW is absent.

A geostrophically balanced slope current, relative to the pressure level at 1700 m depth, is calculated from the hydrographic fields and is imposed along the eastern model boundary (Figures 2b and 2c). Apart from that, the initial momentum fields are at rest. We apply an idealized westerly wind stress over the deep ocean with a sinusoidal decay to zero from $y = 375$ km to the southern boundary (Figure 2). We conduct simulations with wind stress maxima corresponding to wind speeds of 0, 3, 6, 9 and 12 m s⁻¹. From 1957 until present, the average wind speed along the main direction (260°) at Halley Research Station is 3.6 m s⁻¹ with a standard deviation of 6.5 m s⁻¹ [British Antarctic Survey, 2013].

We do not include sea ice in the simulations, but restore sea surface temperature (SST) and salinity (SSS) to mimic the effects of ice. We do not consider tides in the model, but a discussion on the effects of tides is given in section 4. Further details on the forcing and boundary conditions are given in Appendix A.

For each scenario, the model is run for 5 model years (1 year is 360 days) applying constant winter (no fresh surface water) surface stratification, and then for 5 years applying constant summer (including fresh surface water) surface stratification (see Figures 2b and 2c). Average fields from the last model year of winter and summer are used for analysis of hydrography and currents as well as depth-integrated Mean and Eddy Kinetic Energy (MKE/EKE). Eddy fluxes are computed using daily mean fields of velocity and hydrography and are averaged over 1 year.

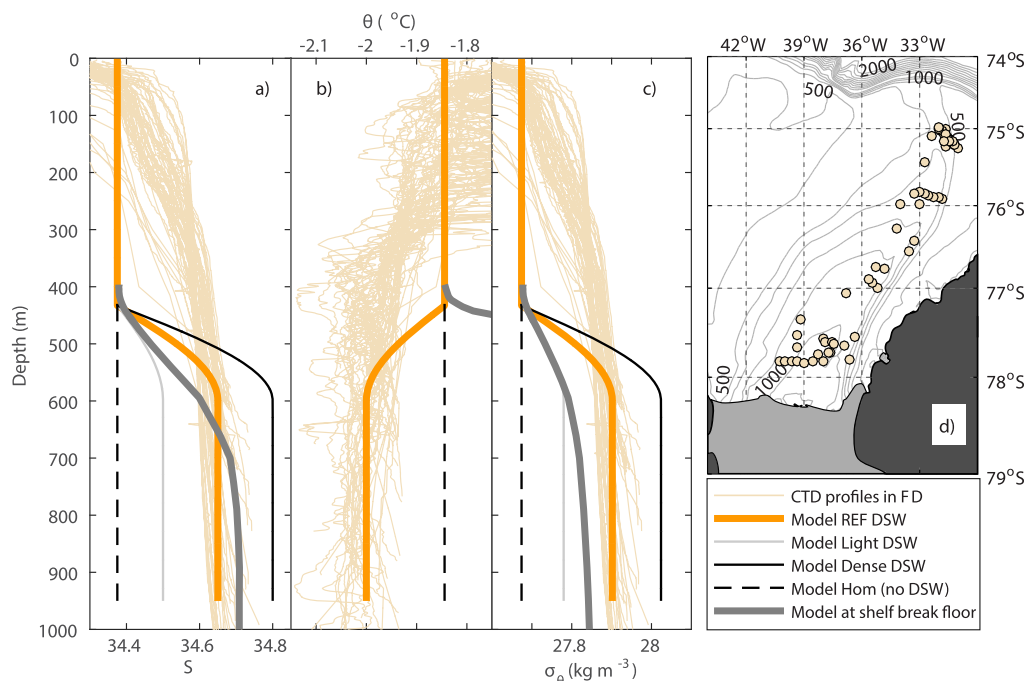


Figure 3. Hydrography from 58 historical CTD profiles in the central, deep Filchner Depression. Thin orange lines show profiles of (a) salinity, (b) potential temperature, and (c) potential density from the locations marked in (d) the map. Modeled trough hydrographic profiles for the REF experiments are shown with thick orange lines. Hydrographic profiles for experiments with perturbed trough density are shown for Light/Dense trough water (thin gray/black lines) and for the Hom experiments with no dense DSW (black dashed lines). The thick, gray lines show the model hydrography at the bottom over the shelf break. The temperature at the shelf break is much warmer than the trough region and exceeds the displayed temperature range.

In addition to the suite of reference simulations, which covers winter and summer scenarios with varying wind forcing, a number of five sensitivity experiments were conducted, where we perturb the trough hydrography (θ_{DSW} and S_{DSW} , Figures 3a–3c) and the wide shelf SSS. An overview of the different experiments and their short names is summarized in Table 1.

2.2. Mesoscale Eddies and Vertical Reynolds Fluxes

To diagnose the effects of eddies in on-shelf heat transport, we follow the methods outlined by *Marshall and Shutts* [1981]. The steady state Eddy Available Potential Energy (EAPE) equation, neglecting sources/sinks of heat and advection of EAPE by eddy velocity, is

$$\bar{\mathbf{v}} \cdot \nabla \frac{\overline{\mathbf{T}^2}}{2} + \overline{\mathbf{v}\mathbf{T}'} \cdot \nabla \bar{\mathbf{T}} + \overline{w\mathbf{T}'} \frac{\partial \bar{\mathbf{T}}}{\partial z} = 0. \quad (1)$$

The overbar represents a time average, long compared to the eddy life time, and the prime represents the deviation from the average. The first term is advection of EAPE by the mean flow. The second term includes

horizontal Reynolds fluxes and represents conversion of mean Available Potential Energy (APE) to EAPE. The third term includes the vertical Reynolds fluxes and represents the conversion of EAPE to Eddy Kinetic Energy (EKE).

In baroclinically unstable regions, away from boundaries, eddies act to reduce the large scale APE related to, e.g., geostrophic currents, by transferring the APE into EKE, and hence, redistribute the water masses toward a less energetic

Table 1. Overview of the Model Runs^a

	Wind Speed x (m s^{-1})	DSW Salinity	Wide Shelf SSS	Short Name
REF	0, 3, 6, 9, 12	34.65 ^b	34.4 ^b	WxREF
SSS Sensitivity	3, 6, 9	34.65 ^b	34.3	WxLowSSS
	3, 6, 9	34.65 ^b	34.5	WxHighSSS
DSW Sensitivity	3, 6, 9	34.40	34.4 ^b	WxHom
	3, 6, 9	34.50	34.4 ^b	WxLight
	3, 6, 9	34.80	34.4 ^b	WxDense

^aAll runs are in pairs of winter and summer. The stars denote reference values. The x in the short names are to be replaced by the wind speed.

^bReference value.

state. The loss of EAPE from conversion to EKE and from advection downstream (positive term 1 and 3 of equation (1)) leads to down-gradient transfer of heat ($\overline{\mathbf{v}'T'} < 0$). *Gent and McWilliams* [1990] have suggested that the eddy fluxes in essence work as an along-isopycnal diffusion operator which tends to make the isopycnals more parallel.

In regions of eddy decay, however, the conversion to EKE is small, or even negative, which can lead to upgradient transfer of heat [*Marshall and Shutts*, 1981]. Similarly, in proximity to boundaries, such as the continental slope, the slope current is restricted to follow f/H contours due to potential vorticity conservation. Here eddies can interact with topography and cause local up-slope transport of denser water (in our case WDW) and hence increase the APE locally [*Nøst et al.*, 2011; *Hattermann et al.*, 2014].

Diagnosing eddy fluxes is not trivial. Ideally, eddy fluxes can be separated into purely rotational and purely divergent parts in order to better understand effects of mesoscale eddy activity [*Marshall and Shutts*, 1981]. However, *Fox-Kemper et al.* [2003] asserted that such a decomposition is only possible in infinite domains. For an open-bounded finite domain, the divergent and rotational fluxes cannot be observed individually, and without using additional constraints these fluxes and their boundary conditions cannot be uniquely determined.

Here we use the vertically integrated, and hence uniquely determined, Reynolds fluxes that represent the conversion of EAPE to EKE (third term in equation (1)), assuming that EAPE is essentially provided by the second term in equation (1). Principally, the vertical Reynolds fluxes are general measures of the transient vertical buoyancy advection and are not related to eddies or any particular mechanism. However, considering that the constant mean model forcing does not introduce any transients, as well as assuming that the interior circulation is nearly adiabatic, i.e., that the grid scale mixing should be small compared to the resolved tracer advection, we can assume that the diagnosed covariance is mainly determined by the internal model variability arising from instability of the forced mean flow. Then, given the temporal (1–360 day band) and spatial ($L \geq 1.5$ km, $H \geq 10$ m) scales taken for the fluctuating terms, we are filtering for what would be a typical signal of mesoscale eddies, although any other type of fluctuations or waves may also be present.

The total vertical flux can be written as the sum of a mean and a fluctuating part (Reynolds flux). For example, for temperature we have

$$\overline{wT} = \bar{w}\bar{T} + \overline{w'T'}. \tag{2}$$

The vertical Reynolds flux is computed as the residual between the two first terms of equation (2). We calculate depth-integrated fluxes of temperature and salinity, and also a linearized density flux, using the approximation:

$$\overline{w'\rho'} = \rho_0(-\alpha \overline{w'T'} + \beta \overline{w'S'}), \tag{3}$$

where ρ_0 is the reference density, α is the thermal expansion coefficient, and β is the saline contraction coefficient. The linearized density aids the understanding of which water masses are involved in the density flux.

Negative Reynolds fluxes for density mean lowering of the APE by lifting light water or lowering dense water. This is expected in most areas of the model, especially away from the steep topography. Positive Reynolds fluxes for density show us where the APE is increased by, e.g., lifting dense water up-slope.

2.3. Potential Vorticity

In order to interpret the interaction of the slope current with the topography of the trough, we will follow the procedure described by *Magaldi et al.* [2011], and calculate the Ertel PV according to equation (4):

$$PV = -\frac{2\Omega + \nabla \times \mathbf{v}}{\rho_0} \cdot \nabla \sigma_\theta \simeq -\frac{f}{\rho_0} \frac{\partial \sigma_\theta}{\partial z} - \frac{1}{\rho_0} \left(\frac{\partial v}{\partial x} - \frac{\partial u}{\partial y} \right) \frac{\partial \sigma_\theta}{\partial z} - \frac{g}{\rho_0^2 f} \left[\left(\frac{\partial \sigma_\theta}{\partial x} \right)^2 + \left(\frac{\partial \sigma_\theta}{\partial y} \right)^2 \right]. \tag{4}$$

We only consider the vertical component of the planetary vorticity, $2\Omega \simeq (0, 0, 2\omega \sin \phi) = f$. We have further applied the thermal wind balance, and neglected the vertical velocity terms [*Hall*, 1994]. The first term on the right-hand side relates to stretching and compression of isopycnals. The second term is related to the relative vorticity, $\zeta = \frac{\partial v}{\partial x} - \frac{\partial u}{\partial y}$ and the last term is connected to tilting of isopycnals.

The model fields have terrain-following vertical coordinates and are interpolated to regularly spaced Cartesian depth levels with $dz = 5$ m before calculation of PV. Finally, the PV is averaged within the isopycnal layer $\sigma_\theta = 27.7\text{--}27.8$, which contains the warm inflow.

3. Results

We will first give an overview of the general model performance (section 3.1). We will then focus on inflow of WDW over the shelf (section 3.2) and into the trough (section 3.3).

3.1. Model Performance

The idealized model approaches a stable state, where the total KE is no longer increasing, after 3–4 years of spin-up for both winter and summer stratification. The circulation pattern agrees with observations in the southern Weddell Sea. A strong, westward slope current is associated with the slope front, with current velocities in the same range as observations from moored instruments [Fahrbach *et al.*, 1992; Jensen *et al.*, 2013] and geostrophic estimates from hydrographic profiles [Heywood *et al.*, 1998]. The slope current and the eddy fields are fully developed ~ 200 km from the eastern boundary. A combination of radiation and nudging along the western boundary efficiently advects the slope current out through the western boundary, and no spurious return flow is seen. In the trough, DSW flows along the eastern flank, crosses the sill to the western flank and leaves the trough (Figures 4a and 4c). The circulation in the trough is similar to recent observations and regional modeling of FD [Darelius *et al.*, 2014], lending some credibility on the idealized model configuration.

In winter scenarios, no warm water is transported onto the shelf, and the shelf water stays homogeneous with temperatures near the surface freezing point (Figure 4a). In summer scenarios, where fresh surface water is present, on-shelf transport of warm water causes increased bottom temperature over the shelf (Figure 4c). The warmest water ($\theta \sim -1.5^\circ\text{C}$) is found in the narrow shelf region, and depth-integrated EKE over the shelf (both narrow and wide) increases by a factor of 10–100 compared to the winter conditions (Figures 4b and 4d).

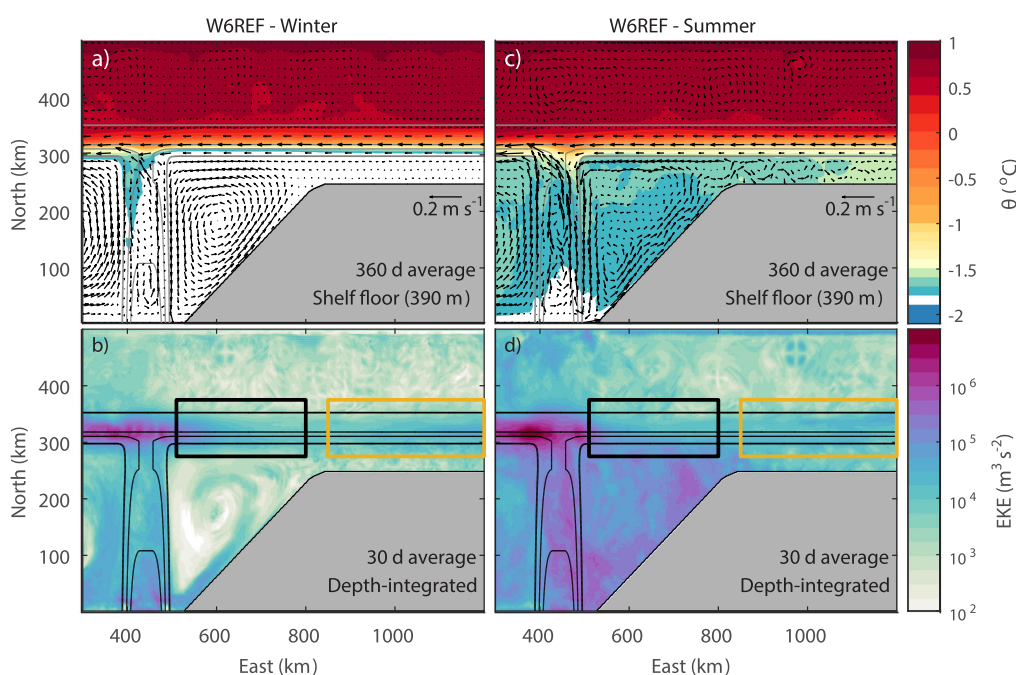


Figure 4. Average temperature and velocity at shelf floor depth (390 m) for W6REF in (a) winter and (c) summer conditions. (b, d) Thirty day averages of depth-integrated EKE during winter and summer conditions, respectively. Isobaths are shown at 450, 600, 800, and 1650 m. Boxes in Figures 4b and 4d indicate the regions for wide (yellow) and narrow (black) shelves discussed in section 3.2.1.

For weak wind scenarios (W0REF and W3REF), the slope current flows westward, along the 850 m isobaths (~ 320 km North), with a core of 0.15 m s^{-1} (Figure 5a). Observations of current velocity across the ASF are limited but reported long-term means range from 0.1 to 0.2 m s^{-1} at slope depths of 400 – 1000 m [Fahrbach et al., 1992; Heywood et al., 1998; Jensen et al., 2013]. In agreement with observations from Fahrbach et al. [1992], the model also shows increasing westward transports associated with the slope current when the wind stress increases. At 900 km East, the westward transport is, relative to W0REF, 100%, 107%, 121%, and 166%, for W3REF, W6REF, W9REF, and W12REF, respectively.

In weak wind scenarios, the core of the slope current follows the 850 m isobath until it reaches the trough mouth region. Here the current crosses the trough mouth while shifting southward, continuing along the 600 m isobath (310 km North, Figure 5a). In scenarios with stronger wind, an additional westward wind-driven current, associated with the Ekman circulation, develops and combines with the initial slope current, to form a broader current with a dual core and weaker maximum velocities (Figures 5c and 5e). The northern core along the 850 m isobath crosses over the trough mouth region similar to scenarios with weak wind. The wind-driven, southern core shifts on-shore for stronger wind. At 500 km East, this core is located over the 525 m isobath (305 km North, Figure 5c) in W9REF. The vertical structure of the current is similar for weak and strong wind scenarios, but as the current shifts south toward shallower isobaths, the current

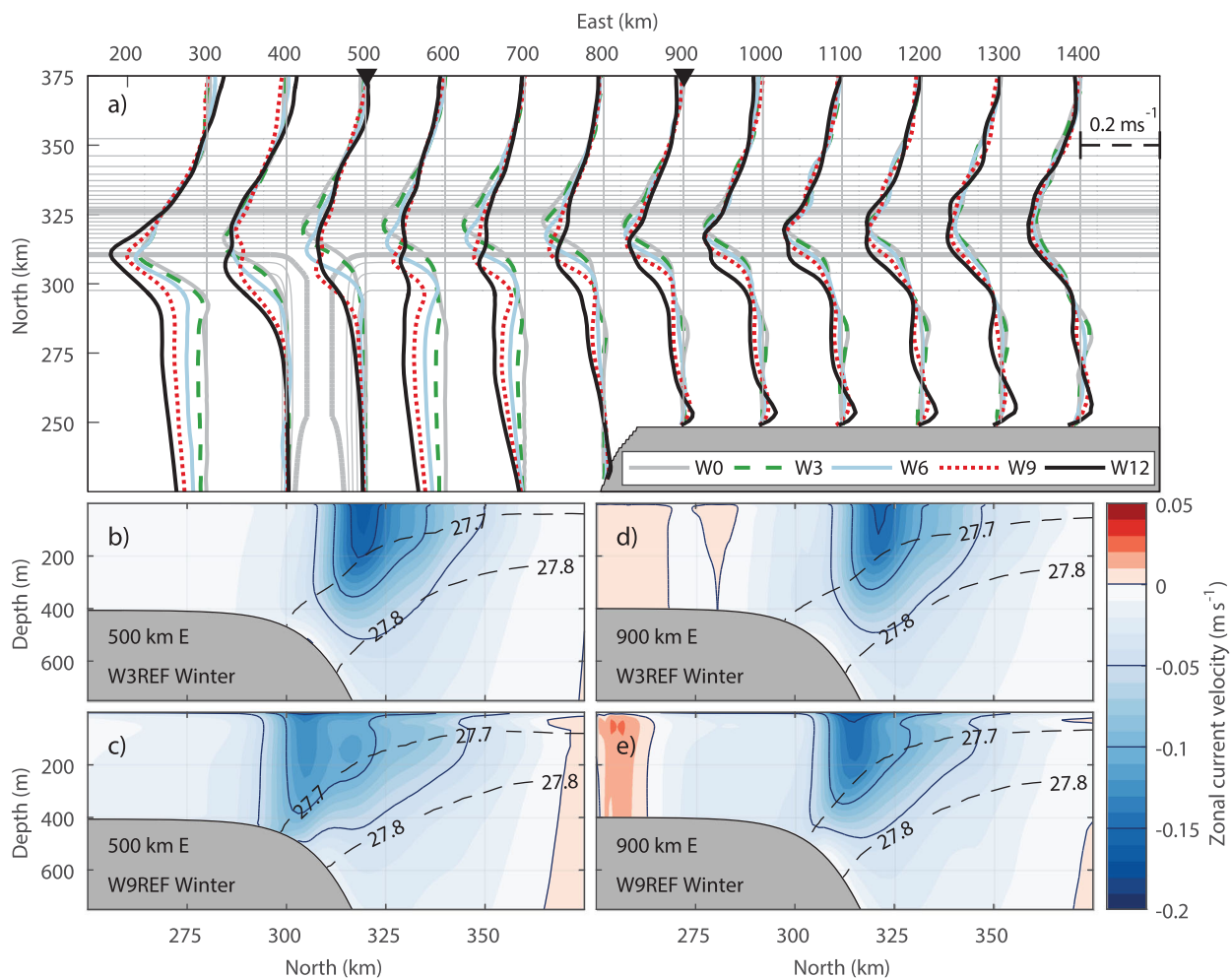


Figure 5. (a) Relative strength of westward slope current for five different wind speed scenarios (see legend for color interpretation) during winter stratification. The distance between the vertical gray lines corresponds to a velocity scale of 0.2 m s^{-1} . Isobaths are shown with increments of 50 m starting at 450 m, where the thick lines correspond to the 500 and 1000 m isobaths, respectively. The black triangles indicate the locations of the vertical transects of zonal velocity shown in (b, c) 500 km East and (d, e) 900 km East. Negative velocities are directed westward. The displayed vertical range is limited to the upper 750 m. The dashed, black lines show the isopycnals $\sigma_\theta = 27.7$ and $\sigma_\theta = 27.8$.

takes up the whole water column and becomes barotropic. The wind-driven part of the current is affected by the trough topography, which affects the inflow of WDW that will be described in section 3.3.

During summer (not shown), the slope current velocity exceeds the winter values near the surface, with maximum velocity $\sim 0.3 \text{ m s}^{-1}$. Comparing to the respective winter wind forcing scenario, the summer transports are 148%, 144%, and 173% for W3REF, W6REF, and W9REF. Over the narrow shelf, a westward coastal current, related to the convergence of fresher surface water along the coast, is found in strong wind scenarios.

In addition to the nonlinear eddy field, the model shows westward propagation of topographic waves along the continental slope. Band-pass filtered Hovmüller diagrams of along-slope currents (not shown) yield waves propagating westward along the continental slope with periods of $\sim 42 \text{ h}$, wavelengths between 80 and 110 km, and with phase speeds between 0.55 and 0.75 m s^{-1} . We do not see wave propagation in the trough, although other model studies indicate that waves can cause considerable onshore heat transport within troughs [St. Laurent *et al.*, 2013]. The waves follow the continental slope and cross the trough mouth region. In the weak wind scenario (W3REF), when the eddy field is weak, the waves account for 95% of the EKE in the model (calculated from EKE frequency spectra in the frequency band 38–51 h). For stronger wind, nonlinear eddy processes and current instabilities become increasingly more important and the wave contribution to the EKE reduces to 50% in W9REF.

To summarize, the modeled flow pattern agrees with observations in the area. The location and the shape of the slope current depend on the strength of the zonal wind stress. A wind-driven component of the slope current, related to the Ekman dynamics, develops for strong winds. In summer, the surface current is stronger and the EKE level is higher over the continental shelf. In section 3.3, we will look further into how the location of the slope current influences the inflow of WDW into the trough region. We will also explore how the density of the DSW within the trough affects the cross-slope exchanges. But before doing so, we examine the role of eddies for the cross-slope exchange over the narrow and wide shelf region.

3.2. Interaction of the Slope Current and the Continental Shelf Break

3.2.1. Eddy Transports Over the Narrow and Wide Shelf Regions

In this section, we will study the balance between the wind-driven Ekman overturning and the counteracting eddy overturning. We will use the Reynolds flux calculations (section 2.2) to examine the cross-slope exchange in a narrow shelf region, and how it changes downstream, when the shelf widens. In the following, the narrow and wide shelf regions will be referred to as narrow/wide regions. We will apply zonal averages over the narrow (yellow) and wide (black) regions identified in Figure 4c. The narrow region is dominated by a convergence of southward Ekman transport at the coastline/ice front, whereas the downwelling is less pronounced in the wide region, where the coastal wall is further away, and the zonal wind stress decays gradually in the wide region (Figure 2a). We will focus on the effect of surface stratification, which changes from winter to summer, and also comment on the effect of wind stress.

The slope current ($> 0.075 \text{ m s}^{-1}$) occupies the water column down to $\sim 400 \text{ m}$, corresponding to the shelf depth, and the location of the slope current core varies with the wind stress as described in section 3.1. In summer, the current becomes more baroclinic with higher surface velocities. We find EKE maxima, coinciding with the slope front in both regions and for both summer and winter stratification (Figures 6a–6d). The EKE is amplified near the surface and the bottom. In summer, higher EKE is also seen near the surface over the flat shelf and upper slope, shoreward of the front.

Being consistent with the EKE structure, the Reynolds fluxes indicate different eddy transports over the wide and narrow shelf in the two seasons. In winter, the vertical density fluxes are always negative across the slope front in the narrow region (Figure 6e). Eddies, dominated by the salt fluxes, act to move fresher water up and more saline water down, suggesting that their main role is to reduce APE by balancing the wind forcing that depresses the isopycnals in this region. In the wide region, the Ekman downwelling ceases and eddy transports will cause a transient response of the weakly forced front, as opposed to a quasi steady state that may be reached in the narrow region. While the integrated net eddy transport is still negative, i.e., reducing total APE, this locally leads to positive density fluxes, as this aids to relax the front (Figure 6f). Also, the total eddy transport is weaker, and the front approaches a more stable

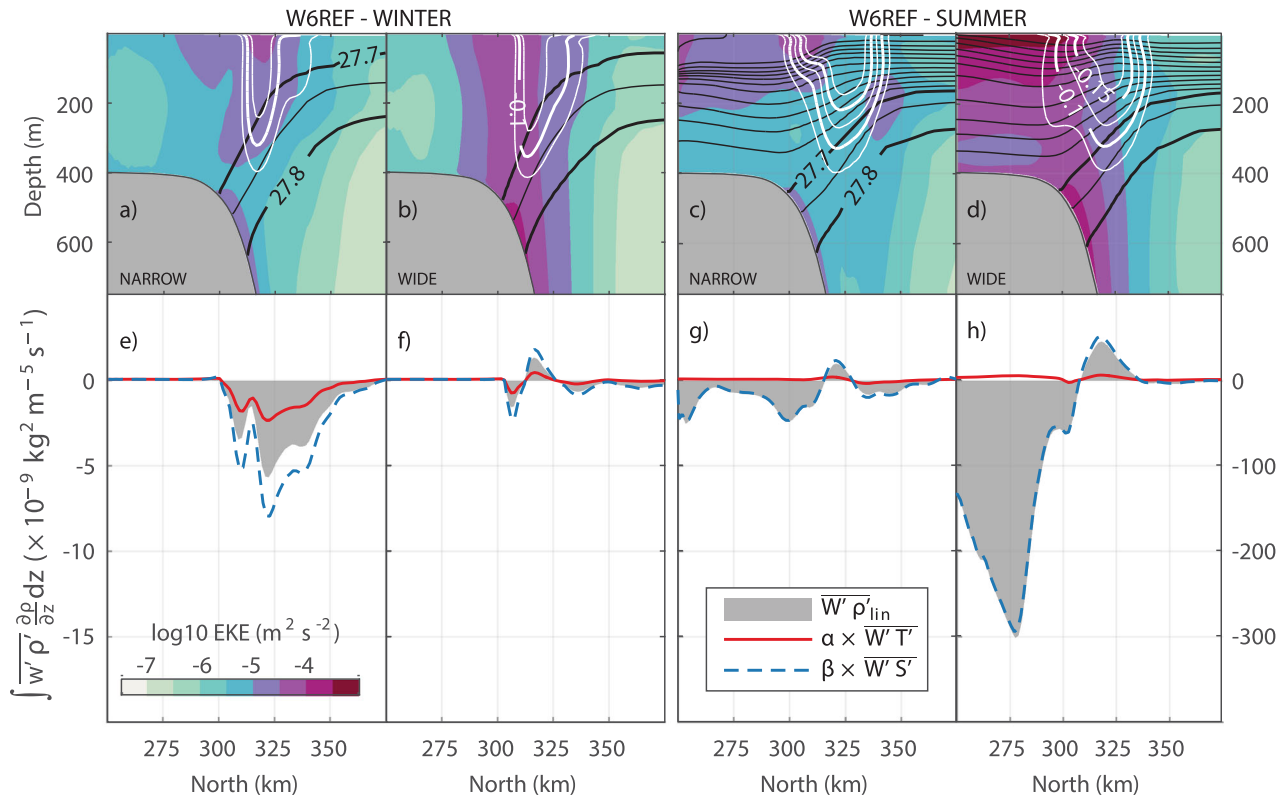


Figure 6. (a–d) Zonally averaged EKE for (a, c) the narrow and (b, d) the wide regions during (a, b) winter and (c, d) summer surface stratification and medium wind stress (W6REF). Black contours show isopycnals with increments of 0.05 kg m^{-3} , and white contours show zonal current velocity in increments of 0.025 m s^{-1} . (e–h) Corresponding depth-integrated vertical Reynolds fluxes (third term in equation (1)) for density (gray filled area), temperature (red), and salinity (blue, dashed). The narrow and wide regions refer to the yellow and black squares in Figure 4c.

configuration with reduced vertical shear of the slope current between 300 and 325 km North in Figure 6f compared to Figure 6e.

In winter, EKE is weak over the flat continental shelf and the Reynolds fluxes vanish accordingly, with no density gradients shoreward of the slope front. In summer, when lighter surface water is present, a second, shallower front develops associated with the near-surface stratification and leads to significant downward density fluxes over the continental shelf. As a result, the Ekman downwelling is balanced by a shallower eddy overturning cell, allowing the deep slope front to relax. This is evident from the vanishing temperature contribution in the Reynolds fluxes (as temperature differences between the fresh surface water and the Winter Water are small) but can also be seen by the shoaling of the $\sigma_\theta = 27.7$ and $\sigma_\theta = 27.8$ isopycnals in (Figure 6d compared to Figure 6b), which leads to warmer water on the shelf in summer, as seen in Figure 4.

3.2.2. Effect of Varying Shelf Salinity

In addition to changes of the surface flow convergence, the shelf water mass properties will also change as the slope current passes from the narrow region, with the less saline Eastern Shelf Water, to the wide region, where more saline and denser waters are observed on the shelf [Gill, 1973]. We will now analyze the effect of along-slope salinity changes on the eddy driven transports. For this purpose, the shelf salinity is modified by increasing/decreasing the SSS restoring value south of 250 km North over the wide shelf region. The narrow region is unaffected by these modifications, since the shelf, in this region, is located north of 250 km North.

In experiments with higher shelf salinity (HighSSS), dense water is exported from the shelf (negative $\overline{W'S'}$ > and $\overline{W'\rho'}$ in Figure 7f). The $\sigma = 27.7$ isopycnal is lifted over the slope (Figure 7d) and forms a V-shape, which connects the cold, dense shelf water to the warmer CDW at middepths over the slope [Stewart and Thompson, 2016]. Eddies transport warm water onto the shelf (positive $\overline{W'T'}$), and the shelf-depth temperature increases by 0.1–0.2°C (Figures 7b and 7f).

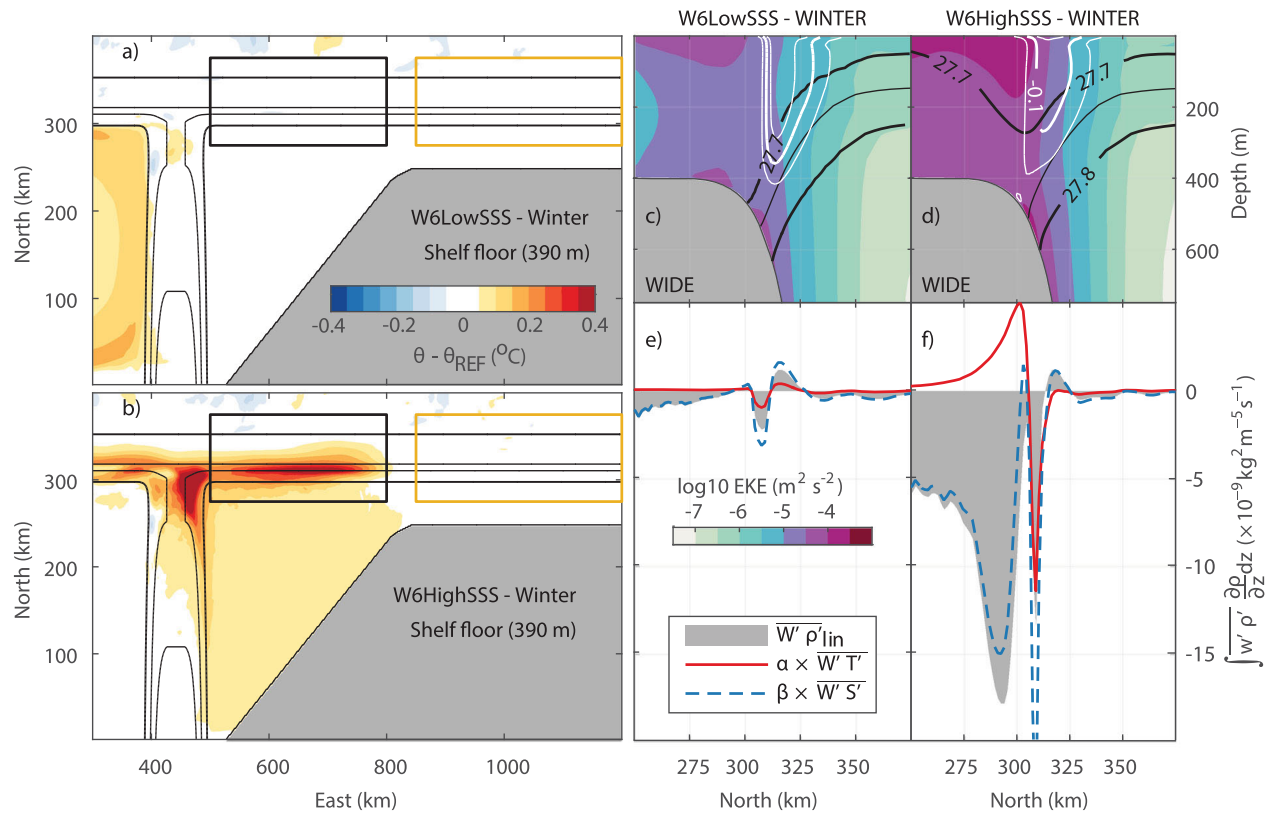


Figure 7. Winter time temperature difference between (a, b) W6LowSSS/W6HighSSS and REFSSS at shelf floor depth (390 m). The yellow and black squares mark the narrow/wide regions, respectively. Isobaths are shown at 450, 600, 800, and 1650 m. (c, d) Zonally averaged EKE for the wide region with (c) lower and (d) higher shelf salinity. Isopycnals are shown with black contours, and white contours show zonal current velocity, where the thicker line is $U = -0.1 \text{ m s}^{-1}$. (e, f) Corresponding depth-integrated vertical Reynolds fluxes for density (gray filled area), temperature (red) and salinity (blue, dashed). The negative salt flux peak (blue line) in Figure 7f is exceeding the axis, with a peak value of $\sim -25 \times 10^{-9} \text{ kg}^2 \text{ m}^{-5} \text{ s}^{-1}$.

In experiments with lower shelf salinity (LowSSS), we find no transport of warm water onto the shelf (Figures 7a and 7e). The shelf water advected from the narrow region is more saline, and negative Reynolds salt fluxes indicate that eddies export this water downslope, reducing the steepness of the $\sigma=27.7$ isopycnal compared to the reference experiment (Figures 6b and 7c).

The effect of changing the shelf salinity is strongest in winter scenarios, when the water mass over the shelf is initially homogeneous. In summer, high eddy activity is connected to the surface stratification as explained above, and the presence of fresh water over the shelf, north of 250 km North, dampens the effect of modifying the water mass salinity over the southern portion of the shelf. Experiments with weaker and stronger wind speed give similar results to the medium wind speed experiment (6 m s^{-1}) shown in Figures 6 and 7.

3.3. Warm Inflow in the Trough

Most observations of warm water entering the Weddell Sea shelf are from areas where bottom corrugations or troughs crosscut the continental slope [Foldvik *et al.*, 1985; Nicholls, 2003; Nicholls *et al.*, 2008; Årthun *et al.*, 2012; Darelius *et al.*, 2016]. In this section, we will study the WDW inflow in an idealized trough with similar geometry to FD.

We will first look at the response to wind stress in the reference scenarios. We will then compare the results to scenarios with modified shelf salinity, to see the effect of the increased shelf-depth temperatures found in the HighSSS scenario (Figure 7b). Finally, we will study how the density of the DSW in the deep trough affects the circulation and inflow of WDW into the trough (Hom/Light/Dense scenarios).

3.3.1. Sensitivity to Wind and Slope Current

In section 3.1, we showed that increased wind stress leads to a stronger and broader slope current. The core of the current is also shifted toward shallower isobaths for stronger wind, and the flow is more affected

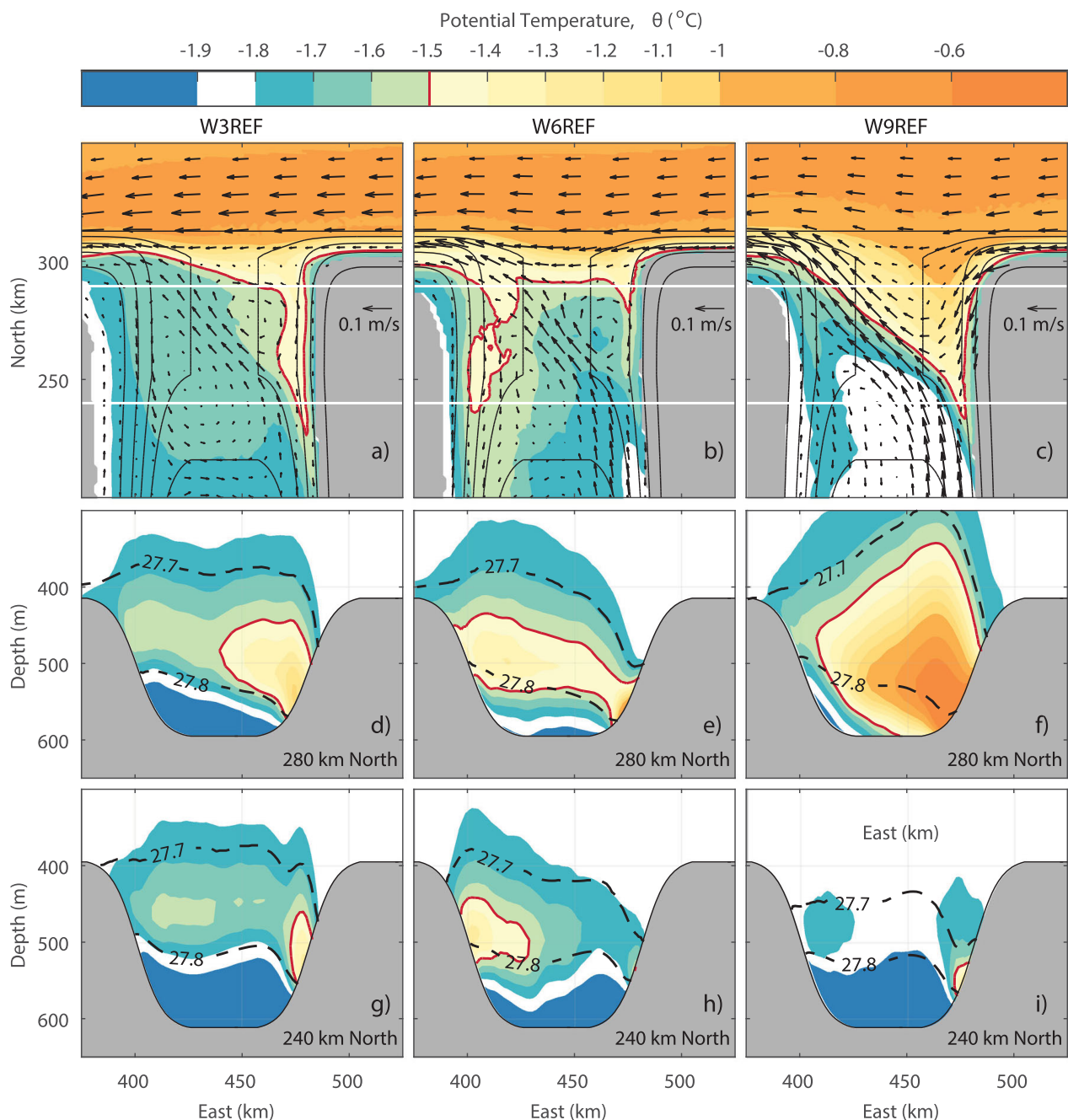


Figure 8. (a–c) Winter temperatures and current vectors in the trough region averaged over densities $\sigma_\theta = 27.7\text{--}27.8$, and vertical sections across the trough at (d–f) 280 km North and (g–i) 240 km North. The transect locations are indicated in Figures 8a–8c by white horizontal lines, and isobaths are shown with 50 m increments from 450 to 650 m. The -1.5°C isotherm is shown with red contours in all plots, and black dotted lines in Figures 8d–8i show the $\sigma_\theta = 27.7\text{--}27.8$ layer.

by the trough topography. In relation to the effect of trough topography and current location, we identify three different regimes of WDW transport into the trough.

The first regime occurs for scenarios with weak wind (W0REF and W3REF). Here the core of the slope current is following the 850 m isobath across the trough and is not affected by the trough bathymetry (Figure 8a). A standing cyclonic vortex on the eastern side of the trough opening draws filaments of warm water south along the eastern side of the trough (Figures 8d and 8g).

The second regime occurs for medium wind (W6REF) when the core of the slope current is following the 620 m isobath. At this location, the current is located at the very corner of the trough opening. The current is deflected at the corner, but the trough topography is weak and the current crosses the trough at 300 km North (Figure 8b). We find that in this regime, a warm inflow into the trough is caused through eddy shedding, as the topographic shelf waves described in section 3.1 interact with the trough opening. From movies of the flow (supporting information I), it can be seen that the waves approximately follow the 650 m isobath and break toward the center of the trough (~460 km East). Examination of the current and the density field shows that those waves cause undulations in the PV field that leads to eddy formation, as described by *Zhang et al.* [2011b]. Being advected by the mean flow, these eddies propagate southwestward across the trough mouth, and into the deep trough, causing warm inflow on the western side of the trough (Figure 8h); a mechanism that appears to be most efficient for intermediate winds.

The third regime occurs during strong wind (W9REF and W12REF), when the trough topography interacts more strongly with the slope current. The wind-driven component of the slope current flows along shallower isobaths and is deflected southward into the trough. Due to PV constraints, the current cannot cross the sill and leaves the trough, along the same path as the outflow of DSW from the deep trough (Figure 8c). The slope current brings large amounts of warm water onto the sill region (Figure 8f), but only a very small amount of this warm water is found south of the sill (Figure 8i). Similar to the second regime, topographic waves break at the trough opening and generate eddies. However, the waves break further east, near the 500 m isobath, and the eddies are mostly being advected out of the trough by the mean current.

The flow pattern described for the three regimes above is also reflected in the time-mean PV fields shown in Figure 9. The PV is low in the slope region for all scenarios and increases over the trough. In the eastern sill area, weaker PV coincide with filaments of WDW inflow. At the southern edge of the sill, where the trough starts to deepen, higher PV forms a barrier which the warm water cannot penetrate. The water column is stretched and conservation of PV leads to gain of cyclonic vorticity, which turns the flow westward over the flat trough bottom. The flow leaves the trough roughly following the topography around the western corner of the trough. In the medium wind scenario (W6REF), the PV barrier appears to be located further north than for the weak and strong wind scenarios (Figure 9b), and the reduced PV along the western side of the trough agrees with more WDW inflow here.

The slope currents response to varying wind strength is similar in winter and summer. However, since the current is wider and less stable in summer scenarios (see EKE in Figures 4 and 6d), eddies interact stronger with the mouth of the trough, such that the first regime is absent, and we find generally more warm inflow than during winter for the comparable wind forcing.

In order to quantify and compare the amount of WDW flowing into the trough, we estimate net mass transports, with positive numbers indicating southward transport, for water masses with $\theta > -1.5^\circ\text{C}$ and $\sigma_\theta > 27.7$ across a transect at 240 km North. Transports are calculated, within the $\theta - \sigma_\theta$ limits, from daily mean

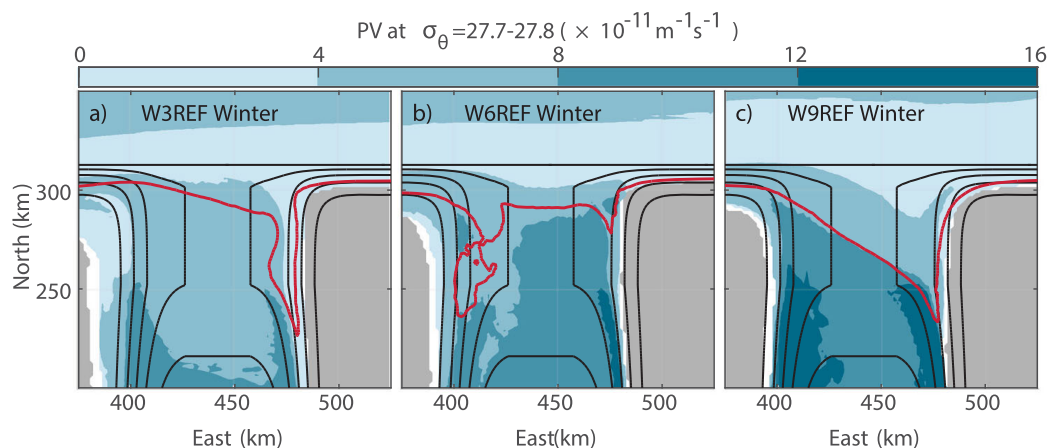


Figure 9. Ertel PV averaged over densities $\sigma_\theta = 27.7 - 27.8$ for the same wind speed scenarios as in Figures 8a–8c. Isobaths at 450–650 m are shown on all plots with increments of 50 m, and the red contour show the -1.5°C .

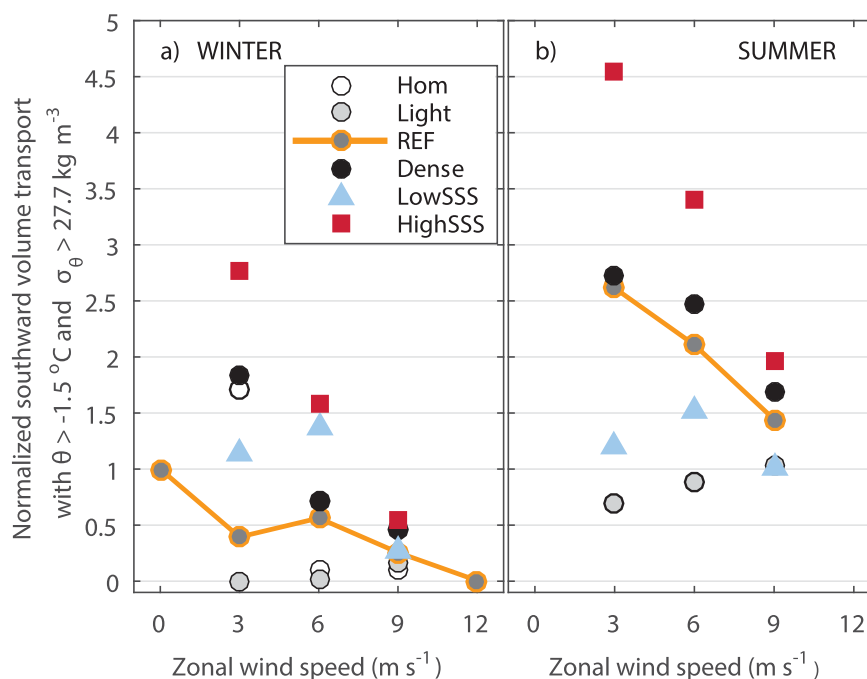


Figure 10. Net southward volume transport across 240 km North for water masses with $\theta > -1.5^\circ\text{C}$ and $\sigma_\theta > 27.7$ for all scenarios, normalized with respect to the W0Ref scenario. Reference scenarios are displayed with orange lines. Different DSW densities are shown with gray-scaled circular markers ranging from white in scenarios without DSW (Hom) to gray and black for increasing DSW densities (Light/REF/Dense). Scenarios with lower (higher) shelf salinity are shown with blue triangles (red squares).

fields to capture transient features, and were then averaged over the last 360 days of the respective model run. For comparison, all estimates are normalized by the transports in the W0REF winter scenario.

Except from the increase in the medium wind winter scenario, which is related to the regime change described above, the southward transport of WDW decreases with increasing wind (orange line in Figure 10) for both winter and summer conditions. The transports are higher in summer compared to winter. In summer, the EKE level is higher (Figure 4d), and we also find increased temperatures for the $\sigma_\theta > 27.7$ water mass (not shown).

3.3.2. Sensitivity to Shelf Salinity and DSW Density

The southward transport of WDW in the trough increases for denser DSW (Dense) and for higher shelf salinity (HighSSS) (Figure 10). The changes are large for the weak wind scenarios, where HighSSS(Dense) bring $\sim 7(5)$ times more WDW into the trough during winter, respectively. For strong wind, changes to the southward transport of WDW are modest, potentially because the strong barotropic flow crossing the trough mouth area prevents weaker baroclinic responses to variations in the hydrography.

In section 3.2, we showed that higher shelf salinity leads to larger Reynolds fluxes and more on-shelf transport of WDW. The $\sigma_\theta = 27.7$ isopycnal was lifted and bent upward over the shelf, forming a V-shape (Figures 7b and 7d). Associated with these changes, the WDW reaches higher up in the water column near the trough opening, and more warm water is hence transported into the trough. For LowSSS, the southward transport of WDW is higher than the reference scenarios in winter and lower than the reference scenarios in summer, for respective wind forcing. Consistent with this result, we find that the EKE levels and Reynolds fluxes increase for LowSSS in winter and decrease in summer (not shown).

In weak wind scenarios (W3), the circulation in the trough amplifies for higher DSW densities and brings more WDW into the trough (Figure 11). The southward transport of WDW is close to zero for W3Light, but is ~ 5 times higher in W3Dense compared to W3REF (Figure 10a). The larger density difference between the DSW and the shelf water sets up a baroclinic flow field that favors the warm inflow (as seen in Figure 11).

When DSW is present in the deep part of the trough, the circulation in the trough is characterized by outflow along the eastern flank and inflow along the western flank (Figures 11i–11l). When the DSW is absent

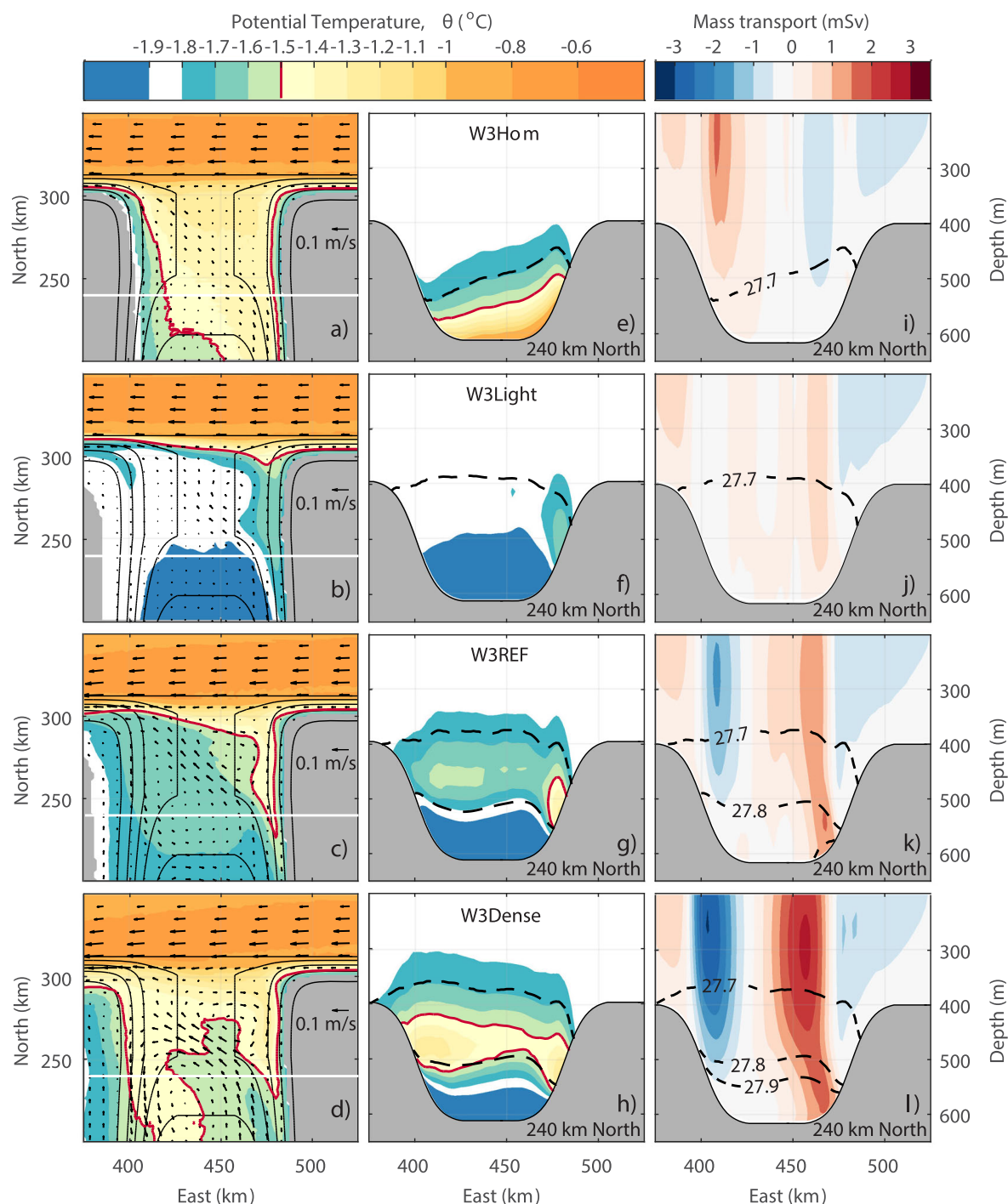


Figure 11. Winter temperatures and current vectors in the trough region averaged over densities $\sigma_{\theta}=27.7\text{--}27.8$ for (a–d) four different DSW densities. Vertical sections of (e–h) temperature and (i–l) mass transport across the trough at 240 km North. The transect location is indicated by white horizontal lines in Figures 11a–11d. The -1.5°C isotherm is shown with red contours in Figures 11a–11h, and black dashed lines in Figures 11d–11l show isopycnals, with increments of 0.1.

(homogeneous shelf and trough), a fundamental circulation change is seen in the trough. In this case, WDW is the most dense water mass in the system and enters the shelf as a gravity current that flows along the bottom of the trough. In the weak wind scenario (W3Hom), the density driven flow in the trough reverses (Figure 11i) leading to warm inflow along the eastern flank. For stronger wind (W6Hom and W9Hom), the circulation pattern is not altered, and there is only small amounts of WDW south of the sill.

4. Discussion

As discussed in section 3.1, our idealized model reproduces the main circulation pattern observed over the continental slope in the Weddell Sea and in FD. The comparison of the different model scenarios has identified several processes that interact to control the access of WDW to the continental shelf and into the trough.

Observations from moored instruments on the Weddell Sea shelf show that warm inflow occurs during the summer season when the thermocline depth is shallower than during winter [Árthun *et al.*, 2012]. *Semper and Darelius* [2016] found changes in thermocline depth on the order of 200 m between winter and summer, upstream of FD, on the narrow continental shelf. Modeled transport of WDW toward the shelf is low for both seasons (summer/winter). We find that the establishment of an upper eddy overturning cell in summer leads to a relaxation of the ASF isopycnals at depth. Since it can be assumed that this process occurs over the entire eastern Weddell Sea, this will lead to a larger shoaling of the thermocline (as observed) than seen in our model results, where the thermocline depth is fixed at the eastern boundary. This is consistent with *Hattermann et al.* [2014] and *Zhou et al.* [2014] who find larger thermocline displacements as a response to surface hydrographic forcing in a periodic (and hence infinite) domain. Running the model with a more realistic summer climatology would likely increase the on-shelf transport of WDW. The increased southward transport of WDW we find during summer scenarios is linked to a dynamic response, rather than to changes in the depth of the thermocline.

Eddy-mediated transport of WDW to the wide continental shelf is most efficient when dense water on the shelf (HighSSS) is transported offshore, creating V-shaped isopycnals across the continental slope. The result agrees with *Stewart and Thompson* [2016], who find that the establishment of an isopycnal connection between the dense shelf water and the CDW, creates a pathway for CDW to access the continental shelf without doing work against the buoyancy force. For the other scenarios, the main role of eddies is to balance the wind-driven downwelling, which influence the thermocline depth and the temperature of the WDW interacting with the trough topography.

The trough, with characteristics similar to FD, contributes to southward transport of WDW in the model. We identify three flow regimes, related to the degree of interaction between the slope current and the trough topography. The response to concurrent effects of mean PV conservation and eddy shedding at the trough opening, is different in the three regimes, and leads to a nonlinear relationship between the wind speed and the southward transport of WDW (Figure 10). In the weak wind regime, there is no interaction between the slope current and the trough topography, and the southward transport of WDW is dominated by eddies. In the medium wind regime, the core of the slope current is located at the edge of the trough opening and is only weakly affected by the topography. However, this regime seems to be optimal for southward transport of WDW by eddies along the western side of the trough. We associate the eddy formation to the blocking of westward propagating topographic waves at the trough opening, as described by *Zhang et al.* [2011b]. The waves propagate westward along the continental slope, supported by the PV jump along the slope. In the strong wind regime, the flow pattern resembles that described by *Williams et al.* [2001], for a shelf break jet flowing over a wide channel topography. The current is deflected southward into the trough but crosses the trough due to PV conservation (compensating vortex stretching and the gain of relative vorticity). The southward transport of WDW is low, but filaments of warm water are transported south along the eastern flank of the trough. Similar to the medium wind regime, eddy formation due to topographic waves and PV undulations occur, but the eddies form closer to the eastern side of the trough, and seem to be efficiently advected out of the trough by the mean current. Movies showing the propagating waves and eddy formation are included in the supporting information.

In summer, the southward transport of WDW in the trough is higher than for winter scenarios with similar forcing. The thermocline response is small (< 50 m), as described above, but we do find higher temperatures within the density layer $\sigma_\theta = 27.7\text{--}27.8$, which leads to larger inflow within the $\theta\text{--}\sigma_\theta$ limits in Figure 10. Furthermore, the EKE level is higher during summer and the southward transport by eddies formed through instabilities in the slope current and breaking of continental shelf waves at the trough mouth is higher. Observations of topographic Rossby waves along the continental slope of the Weddell Sea [*Jensen et al.*, 2013; *Semper and Darelius*, 2016] also show more wave activity and higher EKE in the summer season, compared to the winter season.

Hellmer et al. [2012] suggested that stronger atmospheric stress from a reduced sea ice cover, combined with lower DSW densities can cause a redirection of the slope current into FD, bringing large amounts of WDW into the ice shelf cavities and increasing the basal melt rates. Our process oriented model does not support such a scenario. Instead, we find that for strong wind, the WDW cannot penetrate the sill due to PV constraints, and the WDW leaves the trough regardless of the DSW density. In experiments with lighter DSW the trough circulation is weaker, and less WDW is transported south. For weak wind, however, we find strong southward transport of WDW when DSW is absent (W3Hom), and the circulation in the trough reverses (Figure 11a), supporting the tipping point behavior suggested by *Hellmer et al.* [2017].

The changes in warm water properties and circulation in the trough and their effect on the ice shelf system merit further studies. In this respect, the idealized numerical model results encourage further experiments on the tipping point behavior and sensitivity to suggested future changes in sea ice production, DSW source waters, and imposed fluxes of DSW at the southern model boundary.

In scenarios with strong wind, we find a convergence of the southward transport of WDW. The barotropic flow, steered by the PV conservation, over the trough sill dominates the flow pattern, and modifications of the hydrographic forcing have little effect. In scenarios with weak wind, we find large differences in the southward transport of WDW, where higher salinity on the shelf (HighSSS) and higher DSW density (Dense) favor southward transport of WDW.

Inclusion of tides is beyond the scope of this study. Our focus has been to study isolated forcing mechanisms. Nevertheless, including tides would increase the general level of mixing along the slope, as the upper continental slope is suggested to be a generation site for semidiurnal internal tides, which are trapped by the critical latitude and dissipate their energy along the bottom [*Fer et al.*, 2016]. Enhanced near-bottom tidal mixing at the M2-frequency could also affect the stability of the slope front and the amount of warm inflow over the shelf.

Darelius et al. [2016] suggested that certain combinations of wind (storm events), sea ice concentration, shelf salinity, and summer preconditioning of the slope front and stratification favor on-shelf transport of WDW. They specifically point to the importance of the wind. Warm water, which is episodically lifted onto the outer shelf during summer, can be advected south by the wind-driven coastal current. The southward transport of warm water increases during storm events with wind from NW (favors southward water transport). In this study, we only consider the effect of constant wind forcing. During constant winter or summer forcing, the effect of storms, or a seasonal hydrological cycle, on the inflow will be the subject for a future study.

5. Conclusions

This study presents results from an eddy-resolving, idealized high-resolution ocean circulation model that resembles the circulation in the southern Weddell Sea shelf and slope region, including the interaction of the coastal current with the Filchner Depression.

Warm inflow over the continental shelf is limited by the presence of the ASF. In agreement with *Stewart and Thompson* [2016], we find that on-shelf transport of CDW mainly occurs when dense water formation over the shelf connects the density surfaces between the oceanic CDW and the cold shelf water, and the CDW can access the shelf without doing work against the buoyancy forces.

We find more warm water on the shelf when fresh surface water is present (summer scenarios). A shallower eddy overturning associated with the upper ocean stratification partially balances the Ekman downwelling, such that the WDW interface is relaxed. Future predictions suggest that a warmer and wetter atmosphere will generally lead to a freshening of the upper ocean. Also, reduced sea ice production will weaken the convection, allowing upper ocean stratification to persist during winter. Both effects will favor more warm water onto the shelf through a relaxation of the thermocline.

We study the ASF balance in a transient configuration that includes along-shelf changes of the shelf width. Reduced Ekman downwelling over the wide shelf, compared to the narrow shelf, affects the Reynolds fluxes but does not impose large changes on the cross-slope exchange unless along-flow variations of the shelf water density are included.

Southward transport of warm water in the trough is controlled by several processes: (I) the thermocline depth, regulating the temperature of the water at the depth of the trough sill, (II) the interaction between the slope current and the trough topography, (III) eddy formation through breaking topographic waves at the trough opening, and (IV) density of the water masses in the trough and on the shelf region upstream of the trough. In our results, (II) is dominant for high wind speed, where we find low southward transport of warm water in all scenarios as the WDW will not cross the sill. (III) is important in scenarios with medium wind speed (6 m s^{-1}), causing high transports of warm water into the western side of the trough. For weak and medium wind speed, the inflow is also sensitive to (IV), with greater inflow for denser DSW and for more saline shelf water upstream. The seasonal changes in the depth of the thermocline are small in the model, but the temperature at shelf depth (390 m) increases in summer, and we conclude that the higher trough inflow in summer is a combined response of the processes (I–III).

The sensitivity experiments based on our idealized model have provided new insights on the response of the warm inflow to changing atmospheric forcing and to modifications of DSW properties. *Hellmer et al.* [2012] and *Timmermann and Hellmer* [2013] suggested a future scenario where the slope current is redirected southward along FD, as a consequence of more mobile sea ice and higher momentum transfer between the atmosphere and the ocean. *Hellmer et al.* [2017] further describe a tipping point behavior, where a warm water flushing of the ice shelf cavity leads to a melt water feedback that enhances the shelf circulation and the southward transport of warm water along the trough. Our results suggest a slightly different response to increased wind stress, where the wind-driven part of the slope current is directed southward along the trough opening, but conservation of PV causes the current to turn at the sill and leave the trough. The current is strong and barotropic and reduces the southward transport of warm water by eddies, as the eddies are being advected out of the trough along with the current. This mechanism occurs for strong wind scenarios regardless of the density of the DSW in the trough. Instead, we find an optimal configuration for medium strength wind forcing, where warm inflow related to eddy-shedding appears to be most efficient. In the simulation with weak wind and no DSW present in the trough (W3Hom), we find a reversed circulation pattern in the trough and increased warm inflow. Although we do not include ice shelves or fresh water input from basal melting, the results support the suggested tipping point behavior. If the DSW production is cut off, a continuous inflow of warm water occurs along the bottom of the trough, reaching the southern boundary of the model. However, we did not find similar results in scenarios with stronger wind. Our work therefore emphasizes the need for further studies of these processes and how they are affected by transient changes in the wind pattern and the DSW properties.

Appendix A: Model Boundary Conditions and Surface Forcing

The northern and southern boundaries are treated as closed walls. Along the eastern and western open boundaries, we apply a radiation boundary scheme with restoring toward the initial hydrography and 3-D momentum fields [*Marchesiello et al.* 2001]. For the 2-D momentum, we apply a radiation condition similar to *Flather* [*Flather*, 1976], but adjusted for staggered grids (named *Shchepetkin* in ROMS) and for the free surface we apply *Chapman* explicit conditions [*Chapman* 1985]. We restore temperature, salinity, and velocities at all boundaries, using smoothly increasing relaxation time scales [*Nycander and Döös*, 2003]. An overview of the restoring zones and time scales is given in Table A1. At all boundaries, we apply a 30 km sponge zone, where the diffusivity and viscosity increase smoothly from $1 \text{ m}^2 \text{ s}^{-1}$ in the interior to $3 \text{ m}^2 \text{ s}^{-1}$ at the boundary.

Table A1. Restoring Zones and Inverse Time Scales

	East	West	North	South	Deep West	Deep Trough
T,S						
Restoring zone (km)	30	30	30	24	345	24
Time scale (days)	60	30	30	5	30	1/24
U,V						
Restoring zone (km)	30	30	30	24		
Time scale (days)	60	30	30	5		

In order to reduce piling up of cold and saline DSW overflow west of the trough (downstream), we increased the restoring zone for temperature and salinity in the 10 deepest terrain-following layers west of 350 km East. At the shelf break, this corresponds to water depths below 400 m, increasing to 1300 m over the deeper ocean.

In the deeper part of the trough (>400 m), a reduced restoring time scale maintains the property of the DSW in the southern trough.

We restore SST and SSS to mimic the effects of sea ice. The restoring time scale is 3 days. For winter simulations, we restore to $SST = -1.9^{\circ}\text{C}$ and $SSS = 34.4$ over the whole domain. For summer simulations, we keep the winter conditions over the wide shelf but restore to $SST = -1.5^{\circ}\text{C}$ and $SSS = 33.7$ over the narrow shelf and deep ocean.

The wind stress is calculated from $\tau = -\rho_{\text{air}}C_D U^2$, where $\rho_{\text{air}} = 1 \text{ kg m}^{-3}$ and the drag coefficient $C_D = 0.001$. We apply an idealized westerly wind stress, with $\tau_{\text{max}} = -\rho_{\text{air}}C_D U_{\text{max}}^2$ over the channel and sinusoidal decay to zero from $y = 375 \text{ km}$ to the southern boundary (Figure 2a).

Acknowledgments

This work is supported by the Centre for Climate Dynamics at the Bjerknes Centre and by the Norwegian Research council's FRINATEK program through the project WARM and through the NARE program under the project WEDDELL. Helpful comments and discussions with P.E. Isachsen were greatly appreciated. We thank T. Birkeland for technical support on computing resources. We also thank K. Makinson and one anonymous reviewer for constructive comments that improved this paper. The model output files used for analysis in this paper is available at <https://archive.norstore.no/>, doi: 10.11582/2017.00003.

References

- Allen, S. E., and X. Durrieu de Madron (2009), A review of the role of submarine canyons in deep-ocean exchange with the shelf, *Ocean Sci. Discuss.*, 6(2), 1369–1406, doi:10.5194/osd-6-1369-2009.
- Árthun, M., K. W. Nicholls, K. Makinson, M. A. Fedak, and L. Boehme (2012), Seasonal inflow of warm water onto the southern Weddell Sea continental shelf, Antarctica, *Geophys. Res. Lett.*, 39, L17601, doi:10.1029/2012GL052856.
- British Antarctic Survey (2013), *UK Antarctic Surface Meteorology; 1947–2013, Database, Version 1.0*, Polar Data Cent, Cambridge, U. K.
- Carmack, E. C., and T. Foster (1977), Water masses and circulation in the Weddell Sea, in *Polar Oceans, Proceedings of the Polar Oceans Conference, Montreal, 1974*, pp. 151–165, Arctic Inst. of North Am., Calgary, Canada.
- Chapman, D. C. (1985), Numerical treatment of cross-shelf open boundaries in a Barotropic Coastal Ocean Model, *J. Phys. Oceanogr.*, 15(8), 1060–1075, doi:10.1175/1520-0485(1985)015<1060:NTOCOS>2.0.CO;2.
- Darelius, E., K. Makinson, and K. Daae (2014), Hydrography and circulation in the Filchner Depression, Weddell Sea, Antarctica, *J. Geophys. Res. Oceans*, 119, 1–18, doi:10.1002/2014JC010225.
- Darelius, E., I. Fer, and K. W. Nicholls (2016), Observed vulnerability of Filchner-Ronne Ice Shelf to wind-driven inflow of warm deep water, *Nat. Commun.*, 7, 1–7, doi:10.1038/ncomms12300.
- Dupont, T. K., and R. B. Alley (2005), Assessment of the importance of ice-shelf buttressing to ice-sheet flow, *Geophys. Res. Lett.*, 32, L04503, doi:10.1029/2004GL020204.
- Fahrbach, E., G. Rohardt, and G. Krause (1992), The Antarctic Coastal Current in the southeastern Weddell Sea, *Polar Biol.*, 12(2), 171–182, doi:10.1007/BF00238257.
- Fer, I., E. Darelius, and K. Daae (2016), Observations of energetic turbulence on the Weddell Sea continental slope, *Geophys. Res. Lett.*, 43, 760–766, doi:10.1002/2015GL067349.
- Flather, R. (1976), A tidal model of the northwest European continental shelf, *Mem. Soc. R. Sci. Liege*, 10(6), 141–164.
- Foldvik, A., T. Gammelsrød, and T. Tørresen (1985), Hydrographic observations from the Weddell Sea during the Norwegian Antarctic research expedition 1976/77, *Polar Res.*, 3, 177–193.
- Foldvik, A., T. Gammelsrød, S. Østerhus, E. Fahrbach, G. Rohardt, M. Schröder, K. W. Nicholls, L. Padman, and R. A. Woodgate (2004), Ice shelf water overflow and bottom water formation in the southern Weddell Sea, *J. Geophys. Res.*, 109, C02015, doi:10.1029/2003JC002008.
- Foster, T., and E. C. Carmack (1976), Temperature and salinity structure in the Weddell Sea, *J. Phys. Oceanogr.*, 6, 36–44.
- Fox-Kemper, B., R. Ferrari, and J. Pedlosky (2003), On the indeterminacy of rotational and divergent Eddy fluxes, *J. Phys. Oceanogr.*, 33(2), 478–483, doi:10.1175/1520-0485(2003)033<0478:OTIORA>2.0.CO;2.
- Gent, P. R., and J. C. McWilliams (1990), Isopycnal mixing in ocean circulation models, *J. Phys. Oceanogr.*, 20(1), 150–155, doi:10.1175/1520-0485(1990)020<0150:IMIOCM>2.0.CO;2.
- Gill, A. (1973), Circulation and bottom water production in the Weddell Sea, *Deep Sea Res. Oceanogr. Abstr.*, 20(2), 111–140, doi:10.1016/0011-7471(73)90048-X.
- Hall, M. (1994), Synthesizing the Gulf Stream thermal structure from XBT data, *J. Phys. Oceanogr.*, 24, 2278–2287.
- Hattermann, T., L. H. Smedsrud, O. A. Nøst, J. Lilly, and B. Galton-Fenzi (2014), Eddy-resolving simulations of the Fimbul Ice Shelf cavity circulation: Basal melting and exchange with open ocean, *Ocean Modell.*, 82, 28–44, doi:10.1016/j.ocemod.2014.07.004.
- Hellmer, H. H., F. Kauker, R. Timmermann, J. Determann, and J. Rae (2012), Twenty-first-century warming of a large Antarctic ice-shelf cavity by a redirected coastal current, *Nature*, 485(7397), 225–228, doi:10.1038/nature11064.
- Hellmer, H. H., F. Kauker, R. Timmermann, and T. Hattermann (2017), The fate of the southern Weddell Sea continental shelf in a warming climate, *J. Clim.*, doi:10.1175/JCLI-D-16-0420.1, in press.
- Heywood, K. J., R. A. Locarnini, R. D. Frew, P. F. Dennis, and B. A. King (1998), Transport and water masses of the Antarctic Slope Front system in the eastern Weddell Sea, in *Ocean, Ice, and Atmosphere—Interaction at the Antarctic Continental Margin*, vol. , edited by S. S. Jacobs and R. F. Weiss, pp. 203–214, AGU, Washington, D. C.
- Jacobs, S. (1991), On the nature and significance of the Antarctic Slope Front, *Mar. Chem.*, 35(1–4), 9–24, doi:10.1016/S0304-4203(09)90005-6.
- Jacobs, S., A. Jenkins, C. F. Giulivi, and P. Dutrieux (2011), Stronger ocean circulation and increased melting under Pine Island Glacier ice shelf, *Nat. Geosci.*, 4(8), 519–523, doi:10.1038/ngeo1188.
- Jensen, M. F., I. Fer, and E. Darelius (2013), Low frequency variability on the continental slope of the southern Weddell Sea, *J. Geophys. Res. Oceans*, 118, 4256–4272, doi:10.1002/jgrc.20309.
- Klinck, J. M. (1996), Circulation near submarine canyons: A modeling study, *J. Geophys. Res.*, 101(95), 1211–1223, doi:10.1029/95JC02901.
- Klinck, J. M., and M. S. Dinniman (2010), Exchange across the shelf break at high southern latitudes, *Ocean Sci.*, 6(2), 513–524, doi:10.5194/os-6-513-2010.
- Magaldi, M. G., T. W. N. Haine, and R. S. Pickart (2011), On the nature and variability of the East Greenland Spill Jet: A case study in summer 2003, *J. Phys. Oceanogr.*, 41(12), 2307–2327, doi:10.1175/JPO-D-10-05004.1.
- Marchesiello, P., J. C. McWilliams, and A. Shchepetkin (2001), Open boundary conditions for long-term integration of regional oceanic models, *Ocean Modell.*, 3(1–2), 1–20, doi:10.1016/S1463-5003(00)00013-5.
- Marshall, J., and G. Shutts (1981), A note on rotational and divergent Eddy fluxes, *J. Phys. Oceanogr.*, 11(12), 1677–1680, doi:10.1175/1520-0485(1981)011<1677:ANORAD>2.0.CO;2.

- Nicholls, K. W. (2003), Water mass modification over the continental shelf north of Ronne Ice Shelf, Antarctica, *J. Geophys. Res.*, *108*(C8), 3260, doi:10.1029/2002JC001713.
- Nicholls, K. W., L. Boehme, M. Biuw, and M. A. Fedak (2008), Wintertime ocean conditions over the southern Weddell Sea continental shelf, Antarctica, *Geophys. Res. Lett.*, *35*, L21605, doi:10.1029/2008GL035742.
- Nicholls, K. W., S. Østerhus, K. Makinson, T. Gammelsrød, and E. Fahrbach (2009), Ice-ocean processes over the continental shelf of the southern Weddell Sea, Antarctica: A review, *Rev. Geophys.*, *47*, RG3003, doi:10.1029/2007RG000250.
- Nøst, O. A., and T. Lothe (1997), The Antarctic Coastal Current-physical oceanographic results from NARE 1996/97, *Norsk Polarinst. Meddelelser 148*, edited by J. G. Winther, pp. 51–57, Norsk Polarinstitutt, Tromsø, Norway.
- Nøst, O. A., M. Biuw, V. Tverberg, C. Lydersen, T. Hattermann, Q. Zhou, L. H. Smedsrud, and K. M. Kovacs (2011), Eddy overturning of the Antarctic Slope Front controls glacial melting in the eastern Weddell Sea, *J. Geophys. Res.*, *116*, C11014, doi:10.1029/2011JC006965.
- Nycander, J., and K. Döös (2003), Open boundary conditions for barotropic waves, *J. Geophys. Res.*, *108*(C5), 3168, doi:10.1029/2002JC001529.
- Orsi, A. H., and C. L. Wiederwohl (2009), A recount of Ross Sea waters, *Deep Sea Res., Part II*, *56*(13–14), 778–795, doi:10.1016/j.dsr2.2008.10.033.
- Paolo, F. S., H. A. Fricker, and L. Padman (2015), Volume loss from Antarctic ice shelves is accelerating, *Science*, *348*(6232), 327–331.
- Pritchard, H. D., S. Ligtenberg, H. Fricker, D. Vaughan, M. van den Broeke, and L. Padman (2012), Antarctic ice-sheet loss driven by basal melting of ice shelves, *Nature*, *484*(7395), 502–505, doi:10.1038/nature10968.
- Rignot, E., S. Jacobs, J. Mouginot, and B. Scheuchl (2013), Ice-shelf melting around Antarctica, *Science*, *341*(6143), 266–270, doi:10.1126/science.1235798.
- Semper, S., and E. Darelius (2016), Seasonal resonance of diurnal continental shelf waves in the southern Weddell Sea, *Ocean Sci. Discuss.*, *13*, 1–25, doi:10.5194/os-2016-36.
- Shchepetkin, A., and J. C. McWilliams (2009), Computational Kernel algorithms for fine-scale, multiprocess, longtime oceanic simulations, in *Handbook of Numerical Analysis*, edited by P. G. Ciarlet, vol. 14, pp. 121–183, Elsevier B. V., doi:10.1016/S1570-8659(08)01202-0.
- St. Laurent, P., J. M. Klinck, and M. S. Dinniman (2013), On the role of coastal troughs in the circulation of warm Circumpolar Deep Water on Antarctic shelves, *J. Phys. Oceanogr.*, *43*(1), 51–64, doi:10.1175/JPO-D-11-0237.1.
- Stewart, A. L., and A. F. Thompson (2015), Eddy-mediated transport of warm Circumpolar Deep Water across the Antarctic Shelf Break, *Geophys. Res. Lett.*, *42*, 432–440, doi:10.1002/2014GL062281.
- Stewart, A. L., and A. F. Thompson (2016), Eddy generation and jet formation on the Antarctic continental slope, *J. Phys. Oceanogr.*, *46*(12), 3729–3750, doi:10.1175/JPO-D-16-0145.1.
- Timmermann, R., and H. H. Hellmer (2013), Southern Ocean warming and increased ice shelf basal melting in the twenty-first and twenty-second centuries based on coupled ice-ocean finite-element modelling, *Ocean Dyn.*, *63*(9–10), 1011–1026, doi:10.1007/s10236-013-0642-0.
- Whitworth, T., A. H. Orsi, S.-J. Kim, W. D. Nowlin Jr., and R. A. Locarnini (1985), Water masses and mixing near the Antarctic Slope Front, in *Ocean, Ice, and Atmosphere: Interactions at the Antarctic Continental Margin*, edited by S. S. Jacobs and R. F. Weiss, AGU, Washington, D. C., doi:10.1029/AR075p0001.
- Williams, W. J., G. G. Gawarkiewicz, and R. Beardsley (2001), The adjustment of a shelfbreak jet to cross-shelf topography, *Deep Sea Res., Part II*, *48*(1–3), 373–393, doi:10.1016/S0967-0645(00)00085-0.
- Zhang, Y., J. Pedlosky, and G. R. Flierl (2011a), Cross-shelf and out-of-bay transport driven by an open-ocean current, *J. Phys. Oceanogr.*, *41*(2004), 2168–2186, doi:10.1175/JPO-D-11-08.1.
- Zhang, Y., J. Pedlosky, and G. R. Flierl (2011b), Shelf circulation and cross-shelf transport out of a bay driven by Eddies from an open-ocean current. Part I: Interaction between a barotropic vortex and a steplike topography, *J. Phys. Oceanogr.*, *41*, 889–910, doi:10.1175/2010JPO4496.1.
- Zhou, Q., T. Hattermann, O. A. Nøst, M. Biuw, K. M. Kovacs, and C. Lydersen (2014), Wind-driven spreading of fresh surface water beneath ice shelves in the eastern Weddell Sea, *J. Geophys. Res. Oceans*, *119*, 3818–3833, doi:10.1002/2013JC009556.